[1] Observing dynamical friction in galaxy clusters

Adhikari, Dalal & Clampitt, arXiv:1605:06688, JCAP 07, 022 (2016)

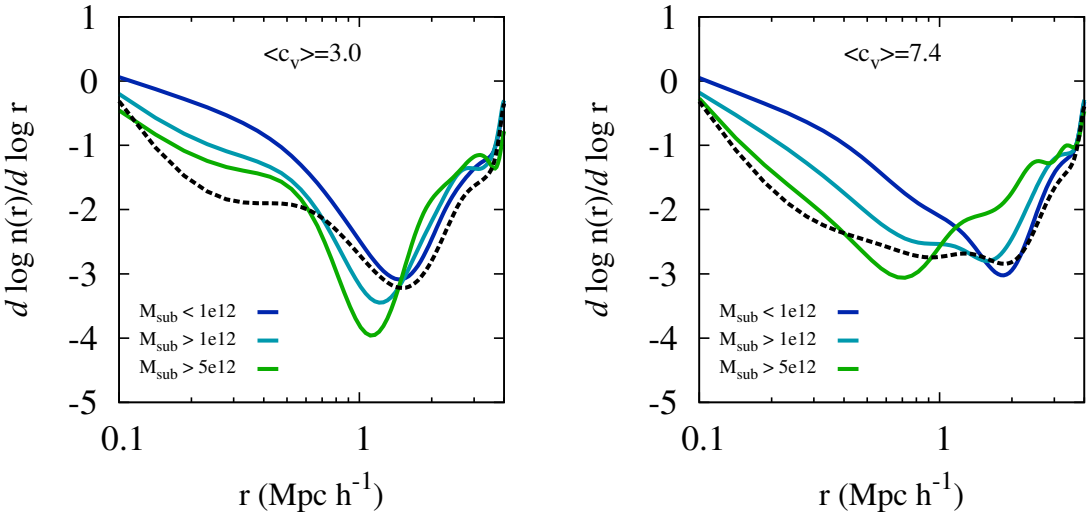

FIG. 1. In both panels, the different curves show the logarithmic slope of the number density profile $d\log n/d\log r$ as a function of radius r within cluster-sized halos of virial mass $M_{\rm host} = 1-4\times10^{14}h^{-1}M_\odot$ from the MDPL2 simulation, for various populations within the host halos. The dashed line corresponds to all dark matter particles, while the solid lines show subhalos of different mass, as denoted in the legend. The splashback radius occurs at the location of the steepening feature in these profiles. Subhalos with less than 1% of the host mass have similar splashback radii as the full set of DM particles, while more massive subhalos have smaller splashback radii, consistent with the effects of dynamical friction. The left panel shows host halos with $c_{\rm vir} < 4$, while the right panel shows host halos with $c_{\rm vir} > 6$, illustrating the significant dependence of dynamical friction effects on host concentrations. Subhalo masses are expressed in units of $h^{-1}M_\odot$.

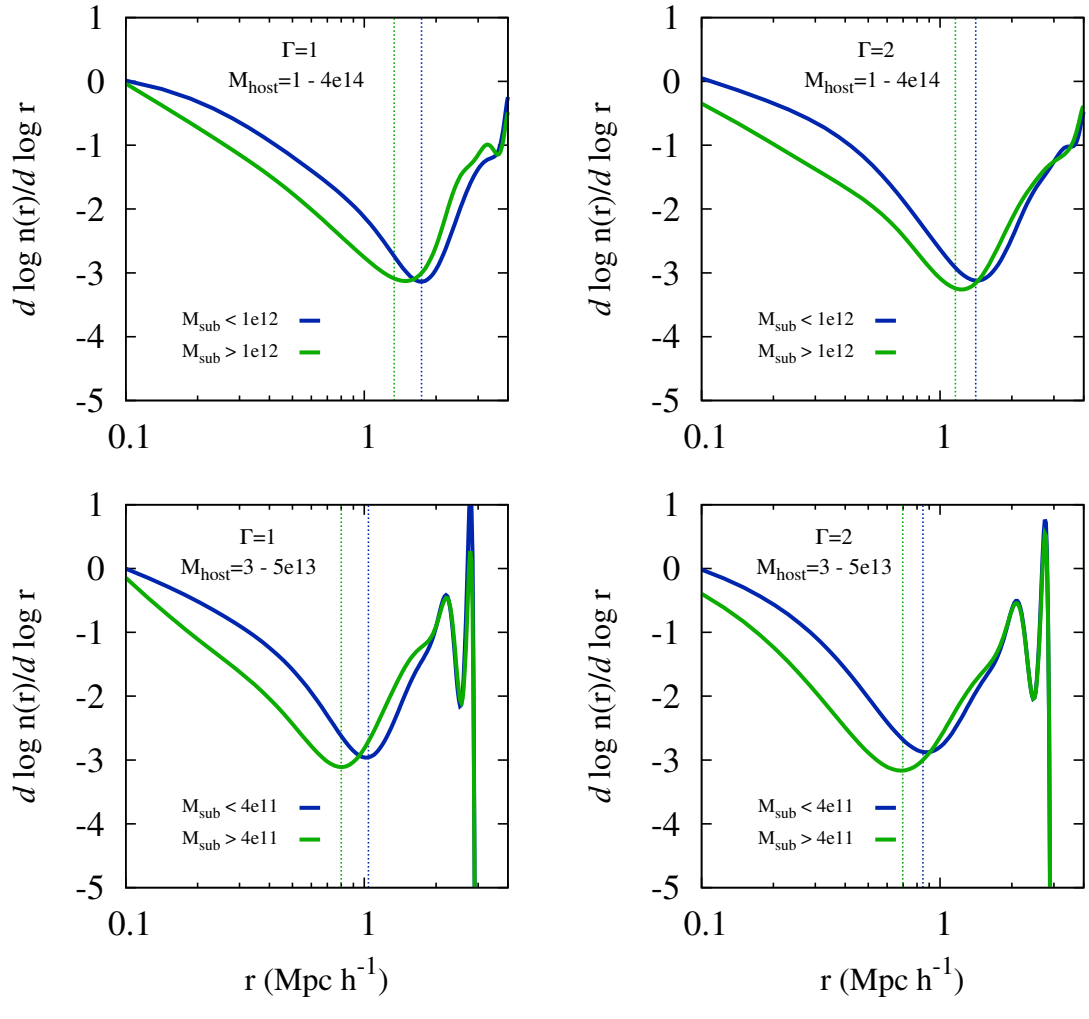

FIG. 2. Shift in the location of splashback due to dynamical friction in subhalos with $M_{\rm sub} > 0.01M_{\rm host}$ in bins of different accretion rate $\Gamma = d\log M_{\rm host}/d\log a$ (left vs. right) and for bins of different host mass $M_{\rm host}$ (top vs. bottom). Halo masses are expressed in units of $h^{-1}M_\odot$. The vertical lines show the prediction from the toy model Eqn. (2). The blue vertical line shows the predicted location in a model without dynamical friction [7], which agrees well with the splashback radius $r_{\rm sp}$ for low mass subhalos where dynamical friction is unimportant. The green vertical line shows the predicted position of splashback from the collapse model with dynamical friction where $\lambda = 1.4$, evaluated at the mean subhalo mass of the sample with $M_{\rm sub} > 0.01M_{\rm host}$.

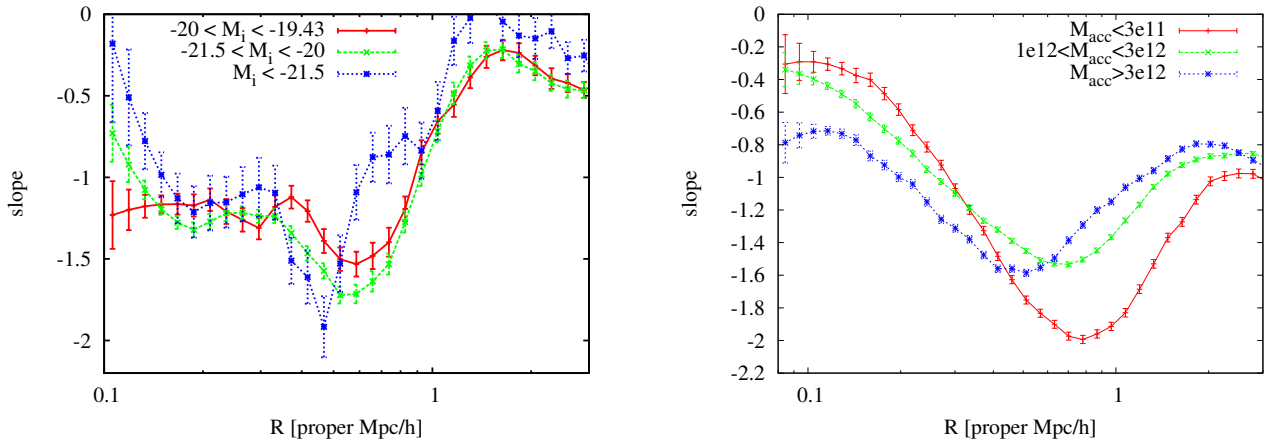

FIG. 3. (Left) Observations of splashback in clusters from the redMaPPer catalog of galaxy clusters with $0.15 < z_c < 0.33$ and $10 < \lambda < 20$. Plotted is the logarithmic slope of the projected number density of galaxies as a function of cluster-centric radius. (Right) Corresponding profiles for subhalos in host halos with $M_{200m} = 3 - 9 \times 10^{13} h^{-1} M_\odot$ at $z = 0.25$ from the MDPL2 simulation. This host mass range was chosen to match the richness range from the left panel. Both panels show the slope of the projected density, not the 3D space density, in contrast to the previous figures.

[2] The halo boundary of galaxy clusters in the SDSS

Baxter, Chang, Jain et al. arXiv:1702.01722

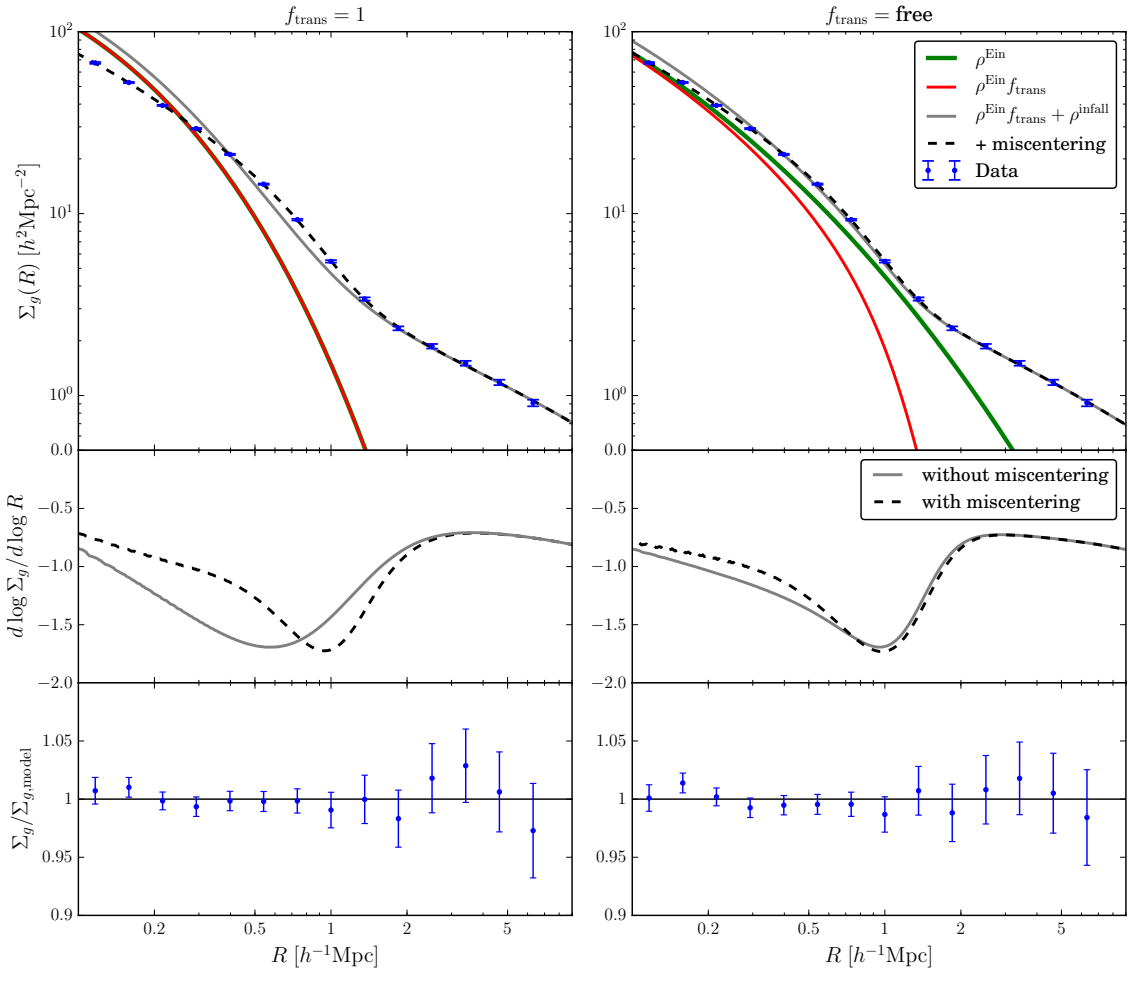

Figure 1. The measured galaxy profile Σ_g around REDMAPPER clusters in SDSS and the corresponding best-fitting models. The top panels show Σ_g measurements and model fits, the middle panels show the logarithmic derivative of the Σ_g models, and the bottom panels show the ratio of the Σ_g data points to the model. The left panels shows the model fits with no steepening function (i.e. $f_{\rm trans} = 1$), while the right panels show the fits with additional steepening beyond an Einasto profile (i.e. $f_{\rm trans}$ is allowed to vary). The red curves in the upper panels show contribution to the projected galaxy density from the collapsed component ($\rho_g^{\rm coll}(r) = \rho^{\rm Ein}(r) f_{\rm trans}(r)$). The green curve in the right panel shows the contribution from the Einasto term of the model ($\rho^{\rm Ein}(r)$). The grey curves are the total profile without miscentering, while the dashed black curves are the profiles with miscentering. Comparing the left and the right panels reveals that a model with large miscentering and $f_{\rm trans} = 1$ can produce very similar total profile as a model with small miscentering and $f_{\rm trans}$ free.

Table 1. Results of model comparison with various modeling and data choices. RM indicates the REDMAPPER catalog, Y07 indicates the catalog of Y07. $\Delta\chi^2$ and $\ln(O_{21})$ values indicate the results of the model comparison between the $f_{\rm trans} = 1$ and $f_{\rm trans}$ = free models, and are computed as described in §3.5.

Model	Catalog	Priors	Scales Fit $[h^{-1}\mathrm{Mpc}]$	$\Delta\chi^2$	$\ln(O_{21})$
A: no miscentering	RM	$f_{\rm mis} = 0.0$, $\tau = 0.0$	$0.1 < R < 8.0$	139	69
B: fixed miscentering	RM	$f_{\rm mis} = 0.2$, $\tau = 0.4$	$0.1 < R < 8.0$	73.3	36
C: miscentering with fiducial prior	RM	$f_{\rm mis} = 0.2 \pm 0.07$, $\tau = 0.4 \pm 0.1$	$0.1 < R < 8.0$	5.2	8.9
D: miscentering with wider prior	RM	$f_{\rm mis} = 0.2 \pm 0.14$, $\tau = 0.4 \pm 0.2$	$0.1 < R < 8.0$	2.6	3.2
E: excluding small scales	RM	$f_{\rm mis} = 0.2 \pm 0.07$, $\tau = 0.4 \pm 0.1$	$0.3 < R < 8.0$	0.8	0.6
F: NFW profile	RM	$f_{\rm mis} = 0.2 \pm 0.07$, $\tau = 0.4 \pm 0.1$	$0.1 < R < 8.0$	42.8	31
G: miscentering with wide priors, tighter prior on α	Y07	$f_{\rm mis} = 0.2 \pm 0.14$, $\tau = 0.4 \pm 0.2$ $\log\alpha = \log(0.2) \pm 0.1$	$0.1 < R < 8.0$	14.1	7.8

Table 2. Best-fit model parameters with $f_{\rm trans}$ free (number preceding semicolon in each column) and $f_{\rm trans} = 1$ (number following semicolon) and under different modeling assumptions. Modeling choices are described in Table 1. We have excluded some parameters in this table for clarity. The remaining parameters are given in Table A1.

Model	Catalog	$r_s[h^{-1}\mathrm{Mpc}]$	$r_t[h^{-1}\mathrm{Mpc}]$	α	β	γ	$f_{\rm mis}$	τ	$R_{\rm sp}^{3D}[h^{-1}\mathrm{Mpc}]$
A	RM	0.85 ; 0.36	1.25 ; —	0.10 ; 0.42	3.83 ; —	6.26 ; —	0.0 ; 0.0	— ; —	1.23 ± 0.05
B	RM	0.32 ; 0.29	1.31 ; —	0.16 ; 0.41	3.71 ; —	6.42 ; —	0.22 ; 0.22	0.32 ; 0.32	1.16 ± 0.05
C	RM	0.27 ; 0.20	1.38 ; —	0.17 ; 0.41	3.98 ; —	6.73 ; —	0.22 ; 0.47	0.34 ; 0.40	1.18 ± 0.08
D	RM	0.24 ; 0.19	1.42 ; —	0.19 ; 0.44	4.11 ; —	6.82 ; —	0.25 ; 0.51	0.34 ; 0.41	1.17 ± 0.09
E	RM	0.35 ; 0.44	1.34 ; —	0.23 ; 0.93	3.66 ; —	6.45 ; —	0.20 ; 0.22	0.42 ; 0.43	1.15 ± 0.07
F	RM	0.79 ; 0.10	1.23 ; —	1.54 ; 0.74	3.65 ; —	6.23 ; —	0.21 ; 0.50	0.45 ; 0.33	1.22 ± 0.17
G	Y07	0.35 ; 0.28	1.30 ; —	0.21 ; 0.38	3.75 ; —	6.20 ; —	0.51 ; 0.48	0.16 ; 0.20	1.16 ± 0.08

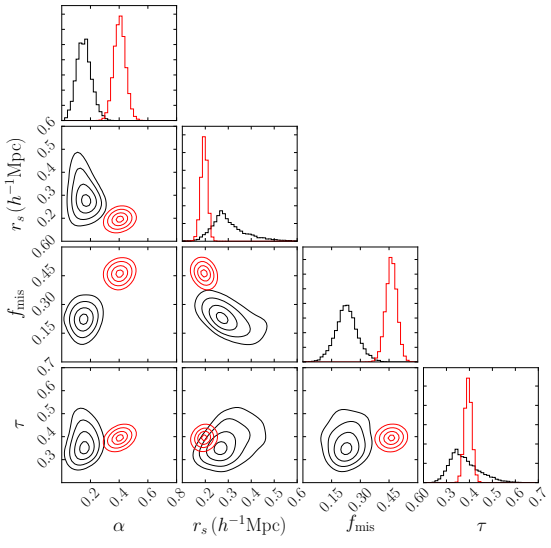

Figure 2. Posteriors on the galaxy profile parameters recovered from the MCMC analysis of the galaxy profile measurements. Black curves show results of analysis that allows the parameters in the $f_{\rm trans}$ term of Eq. 4 to be free, while red curve shows results when $f_{\rm trans} = 1$. Both analyses use the Model C miscentering priors from Table 1.

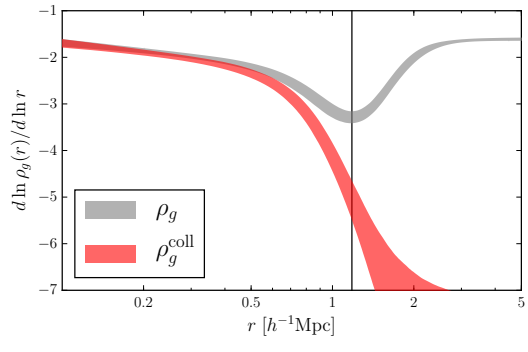

Figure 3. Constraints on the 3D logarithmic derivative of the collapsed component ($\rho_g^{\rm coll}(r)$) and total galaxy density ($\rho_g(r)$) from our model fits to the measured galaxy density profile around REDMAPPER clusters. The best fit value of the splashback radius, $R_{\rm sp}^{3D}$, is shown as the vertical line. The data prefer a profile which exhibits a steepening to slopes significantly steeper than -3 over a narrow range in radius. This finding can be interpreted as evidence for truncation of the halo profile consistent with that seen in simulations by DK14.

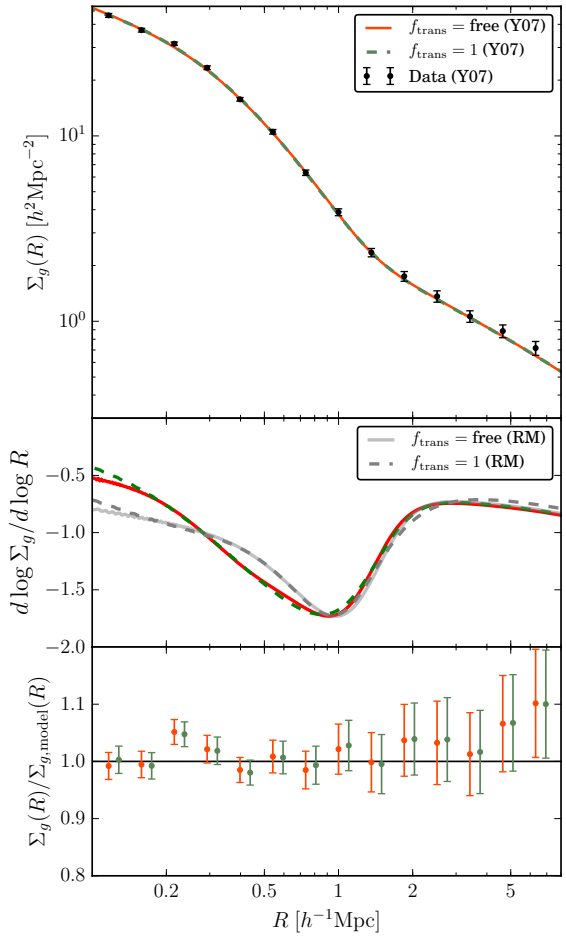

Figure B1. Measurement of the splashback feature using the Y07 group catalog. The top panel shows the projected galaxy density profile Σ_g overlaid with models with $f_{\rm trans}$ free (red solid) and $f_{\rm trans} = 1$ (green dashed). The middle panel shows the log-derivative of Σ_g. We note that the two model fits are nearly identical in both panels. We also overlay in grey the same measurements shown in Fig. 1, which is based on the REDMAPPER (RM) cluster catalog. The feature around 1 h^{-1}Mpc in the REDMAPPER measurements appear slightly sharper than the Y07 group measurement. The bottom panel shows the ratio of the Y07 measurements to the best-fit models.

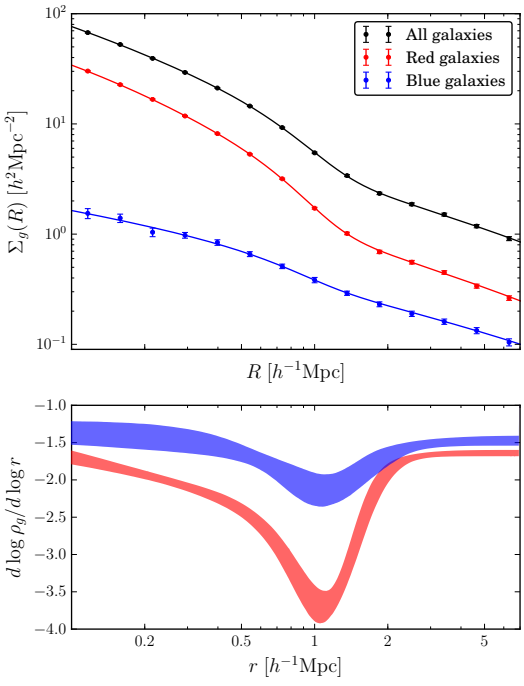

Figure 5. The top panel shows the $\Sigma_g(R)$ measurements for the full sample (black data points), the reddest quartile of galaxies (red data points) and bluest quartile of galaxies (blue points); best fit models to the different measurements are shown as solid lines. The bottom panel shows the corresponding log-derivatives of $\rho_g(r)$ inferred from model fiting.

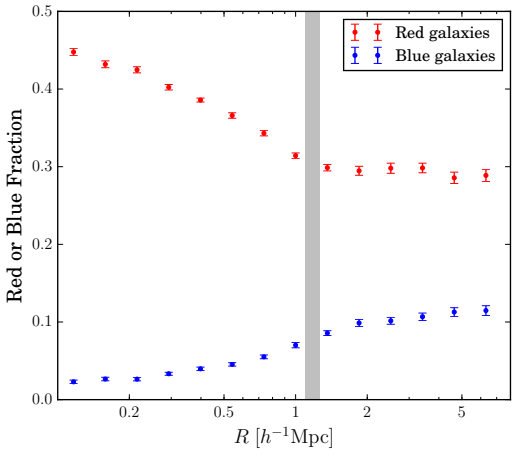

Figure 6. The fraction of red and blue galaxies relative to all galaxies around REDMAPPER clusters as a function of the projected distance from the cluster center.

[3] Splashback shells of cold dark matter halos

Mansfield, Kravtsov & Diemer, arXiv:1612.01531

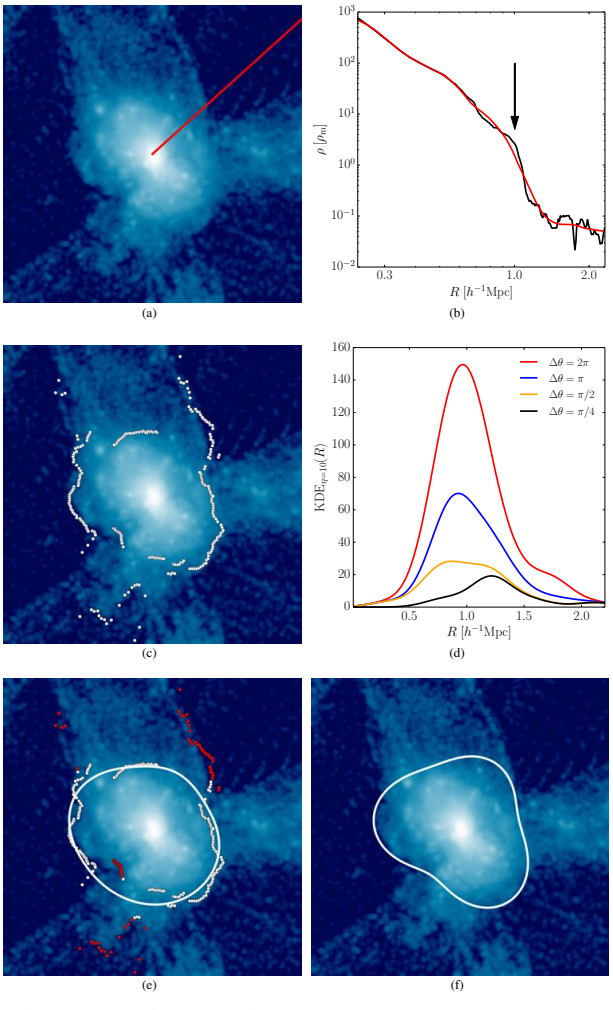

FIG. 1.— An overview of the steps in our shell-finding algorithm for a cluster-sized halo (This halo is also shown in Figure 2(d) below). Figure 1(a) shows a random line of sight traced through this halo's density field (see §2.2.1 and Appendix A). Figure 1(b) shows the density profile along this line of sight before smoothing (black line) and after smoothing with a Savitzky-Golay filter (red line). The arrow indicates the point of steepest slope identified by the algorithm in the smoothed profile (see §2.2.2). Figure 1(c) shows the points of steepest slope for the 256 lines of sight in the viewing plane. Figure 1(d) shows the filtering KDEs for the angular bins containing the highlighted line of sight at different refinement levels (see §2.2.3). Figure 1(e) shows the point classification that the algorithm generates for this point distribution (see Appendix B). The white curve shows the filtering spline created during the point selection process. Points which are close enough to this curve to pass the filter are shown in white and those which are too far away are shown in red. Figure 1(f) shows the cross-section of the best fit Penna-Dines surface from the overall distribution of splashback points from 100 randomly oriented planes in which such a procedure was carried out (see §2.2.4). See the text in the corresponding sections for details. All analysis is done with the parameter values listed in Table 2, but the underlying images are rendered using spherical kernels of radius $0.05R_{200m}$ to make the structures around halos more clear.

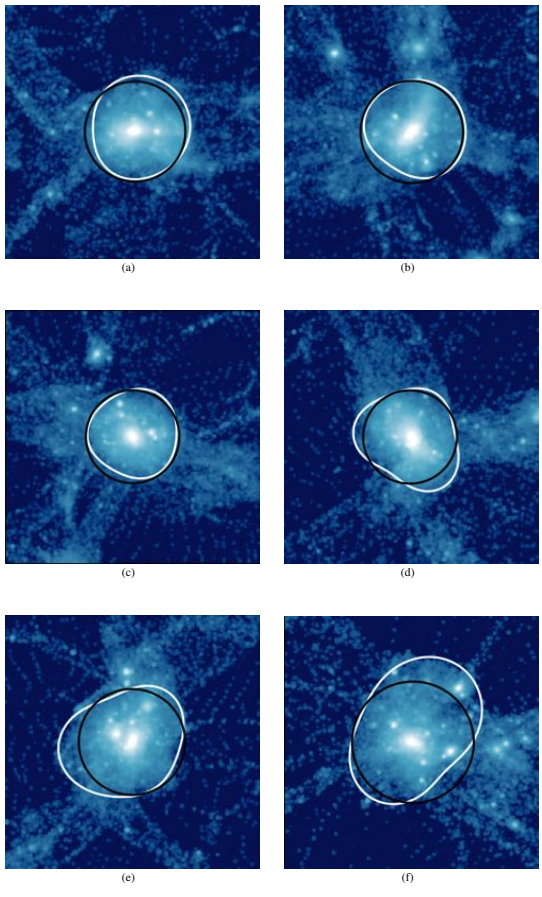

FIG. 2.— Density slices of six halos are shown within boxes of size $5R_{200m}$ along with cross-sections of each halo's splashback shell identified by our algorithm (white lines) and cross-sections of spheres with the same volume as the splashback shell (black circles). The six halos were picked randomly by sampling halos uniformly from within in the the $\log M_{200m} - \Gamma$ plane in our L0063 simulation box. Note that Figure 2(d) shows the halo used to illustrate our algorithm in Figure 1.

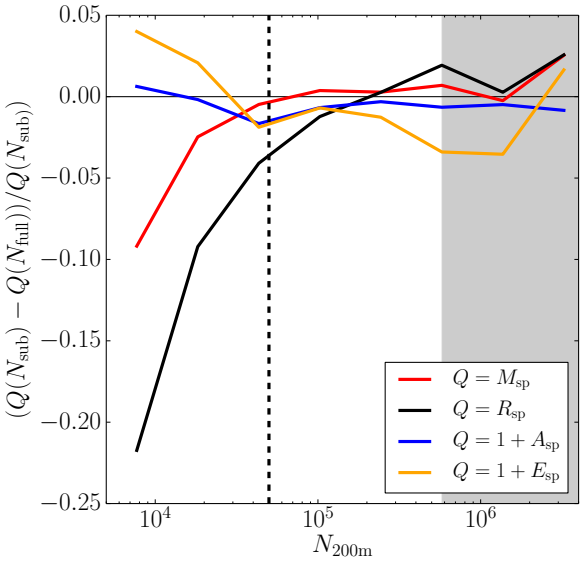

FIG. 3.— Convergence tests for the properties of splashback shells defined in Equation 7 - Equation 11 : enclosed mass, M_{sp}, radius of the sphere of equivalent radius, R_{sp}, ellipticity, E_{sp}, and asphericity, A_{sp} as a function of the number of dark matter particles within R_{200m}, N_{200m}. The vertical dashed line corresponds to $N_{200m} = 50,000$, the lower limit used for the analysis in this paper, and the shaded vertical region indicates bins which contain two or fewer halos and are therefore dominated by individual halo error. Within the converged particle count range there is typically a scatter of $\approx 2\%$ about the median relation, which has not been plotted here for visual clarity. See section 3 for details and discussion on this figure.

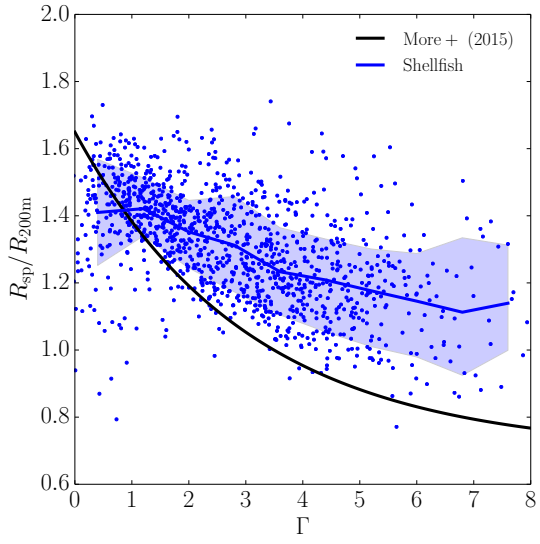

FIG. 5.— Comparison between the distribution of R_{sp}/R_{200m} values measured by SHELLFISH to the prediction of stacked density profile analysis. The black curve shows the best fit to location of steepest slope in the stacked density profiles as a function of accretion rate, Γ. We use the parameterization for this fit reported in More et al. (2015). The blue points show SHELLFISH R_{sp}/R_{200m} measurements for individual halos, the blue curve shows the median measurement, and the blue contours show the 68% envelope. The SHELLFISH curve differs from stacked profiles in both amplitude and shape, becoming ≈30% larger for halos with $\Gamma > 4$. A qualitatively similar difference can be seen at all redshifts. We argue that this difference is due to stacked profiles splashback measurements being artificially biased inwards by massive subhalos in section 4.2.

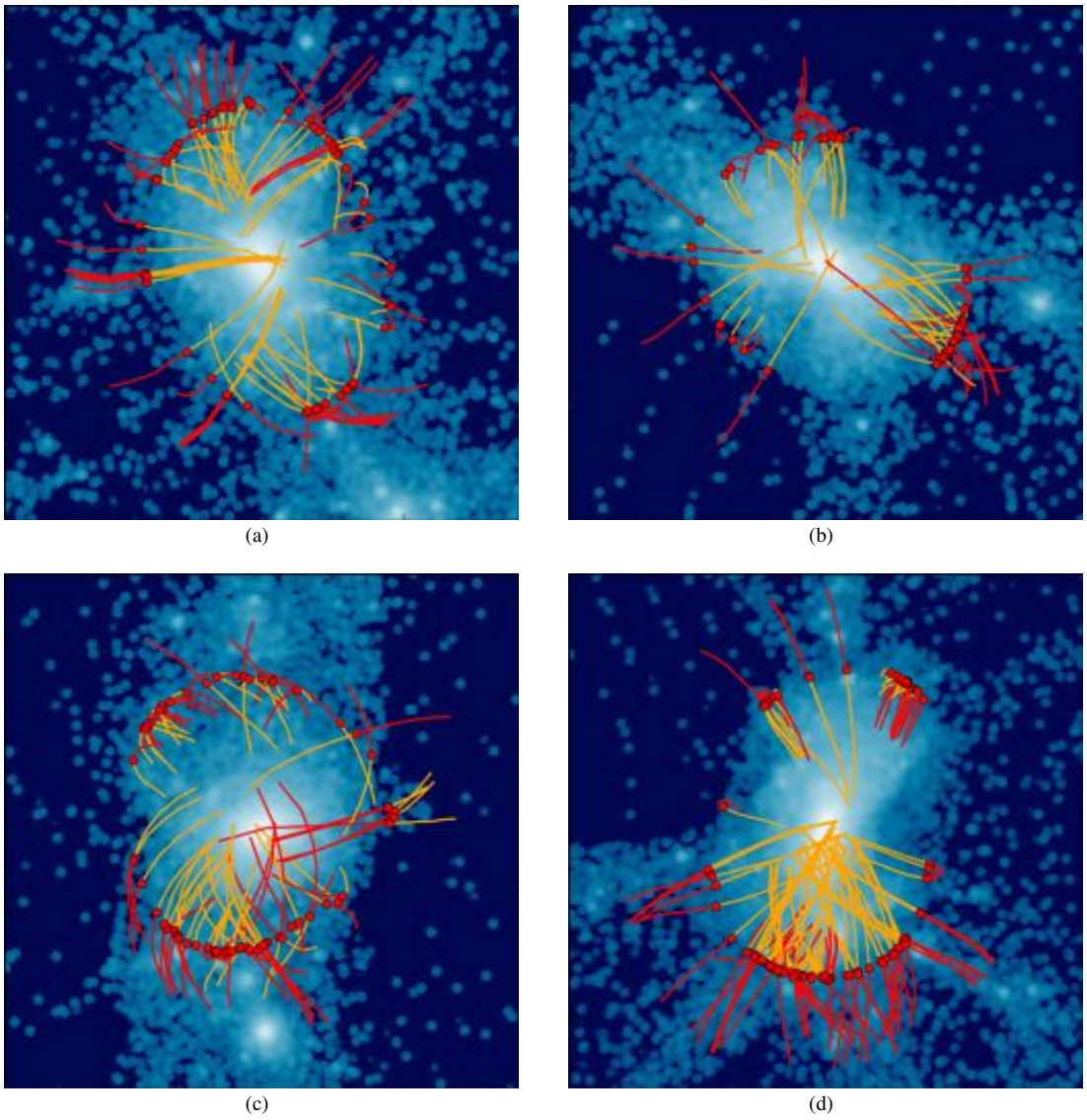

FIG. 4.— Trajectories for particles during the redshift interval $z \in [0.32, 0]$ near the splashback shell of four clusters from the L0250 simulation with $M_{200m} \approx 10^{14} h^{-1}\, M_\odot$ identified at $z_1 = 0.13$. Each figure shows a slice through the density field in a region centered on the halo with a width of $5R_{200m}$ and a depth of $R_{200m}/5$. Every particle in this slice located within $R_{200m}/50$ of the splashback shell identified by SHELLFISH at $z_1 = 0.13$ is shown as a red point. The trajectory of each particle during the redshift interval $[0.31, 0.13]$ is shown by red line, while the trajectory during the redshift interval $[0.13, 0]$ is shown by yellow lines. See section 3.1 for details.

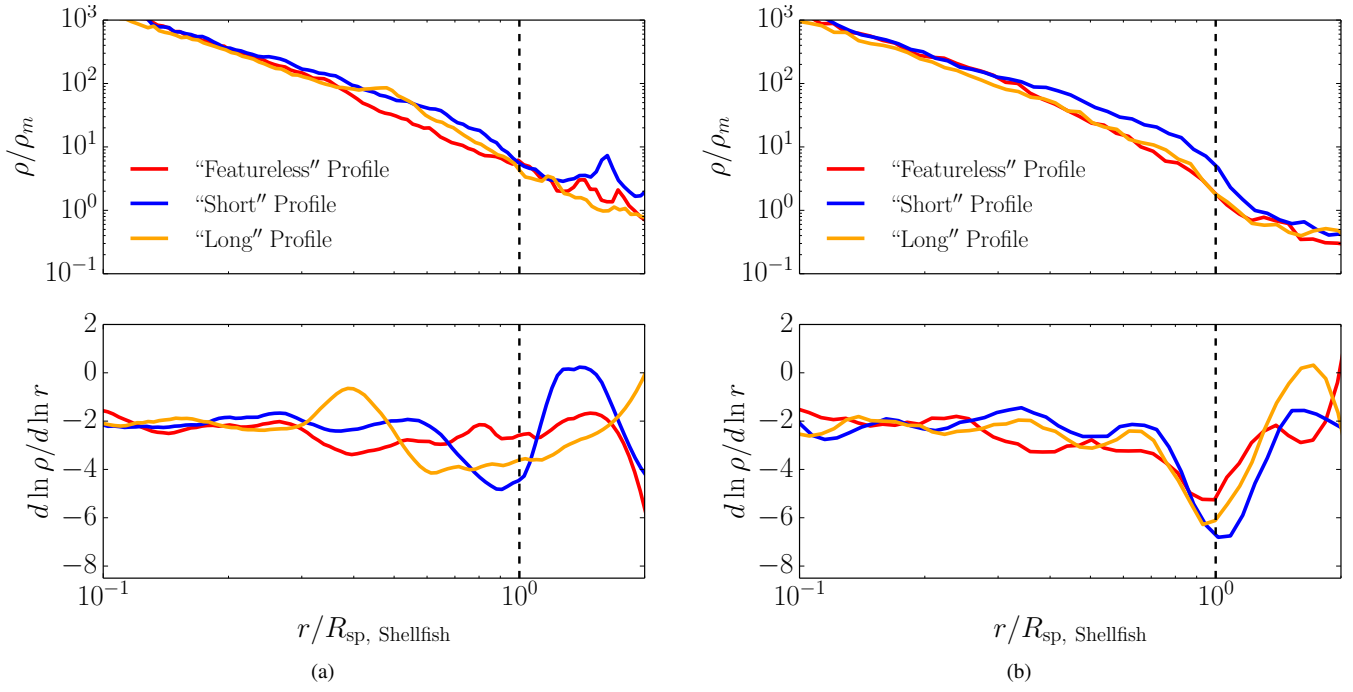

FIG. 6.— Comparison between spherically averaged radial density profiles (Figure 6(a)) and the angular median density profiles described in 4.3 (Figure 6(b)). The top panels show density and the bottom panels show logarithmic slope after the density profiles have been smoothed with a fourth-order Savitzky-Golay filter with smoothing windows a third of a decade wide. Both density and slope profiles have had their radii normalized by $R_{\rm sp}$ as measured by SHELLFISH. The three halos are chosen to be representative of the three qualitative classes of halo profiles we identified in section 4.2. Because angular median profiles are designed to remove interfering substructure, they have deeper and more well-defined points of steepest slope. The level of agreement between the radius of steepest slope of the angular median profiles shown here and the $R_{\rm sp}$ values derived by SHELLFISH is typical.

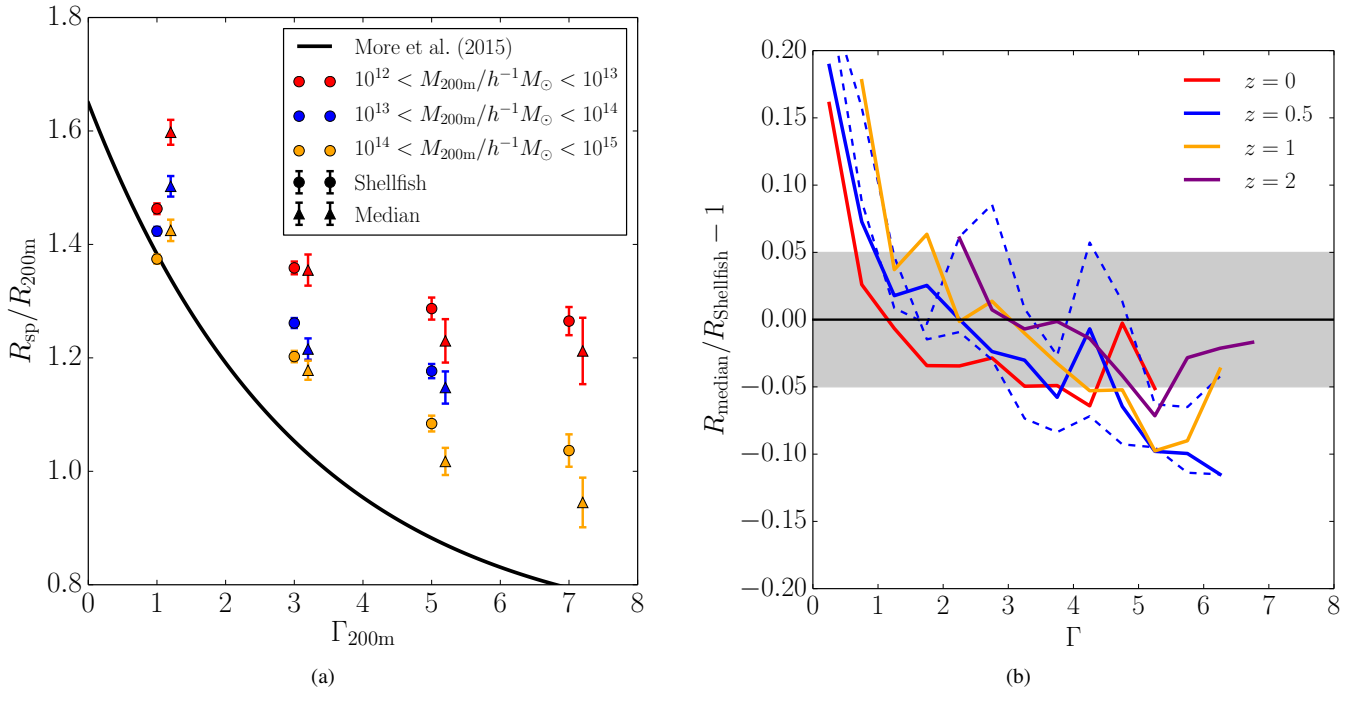

FIG. 7.— Comparison between the mean $R_{\rm sp}/R_{\rm 200m}$ values measured by SHELLFISH and by the angular median profile method described in section 4.3. The left panel shows measurements made by the two methods for different Γ and $M_{\rm 200m}$ bins at $z = 0.5$. Shellfish measurements are shown as circles on the left side of their respective Γ bins, and angular median profile measurements are shown as triangles on the right side of their respective Γ bins. Error bars represent only the bootstrapped error on the mean and do not account for known systematic uncertainty in the angular median profile method (see section 4.3). The right panel shows the median value of $R_{\rm Shellfish}/R_{\rm median} - 1$, for every halo in our sample at $z = 0$, 0.5, 1, and 2. The dashed blue lines show the shape of this curve when the angular median profile's Savitzky-Golay window width is varied to the edges of its physically reasonable value range to give a sense of the systematic variability in this method (see section 4.3). These two figures illustrate that when large subhalos are removed from the density profiles of halos, the location of the point of steepest slope becomes consistent with the value of $R_{\rm sp}$ measured by SHELLFISH. They also illustrate that there is a non-trivial disagreement between the two methods for very small Γ.

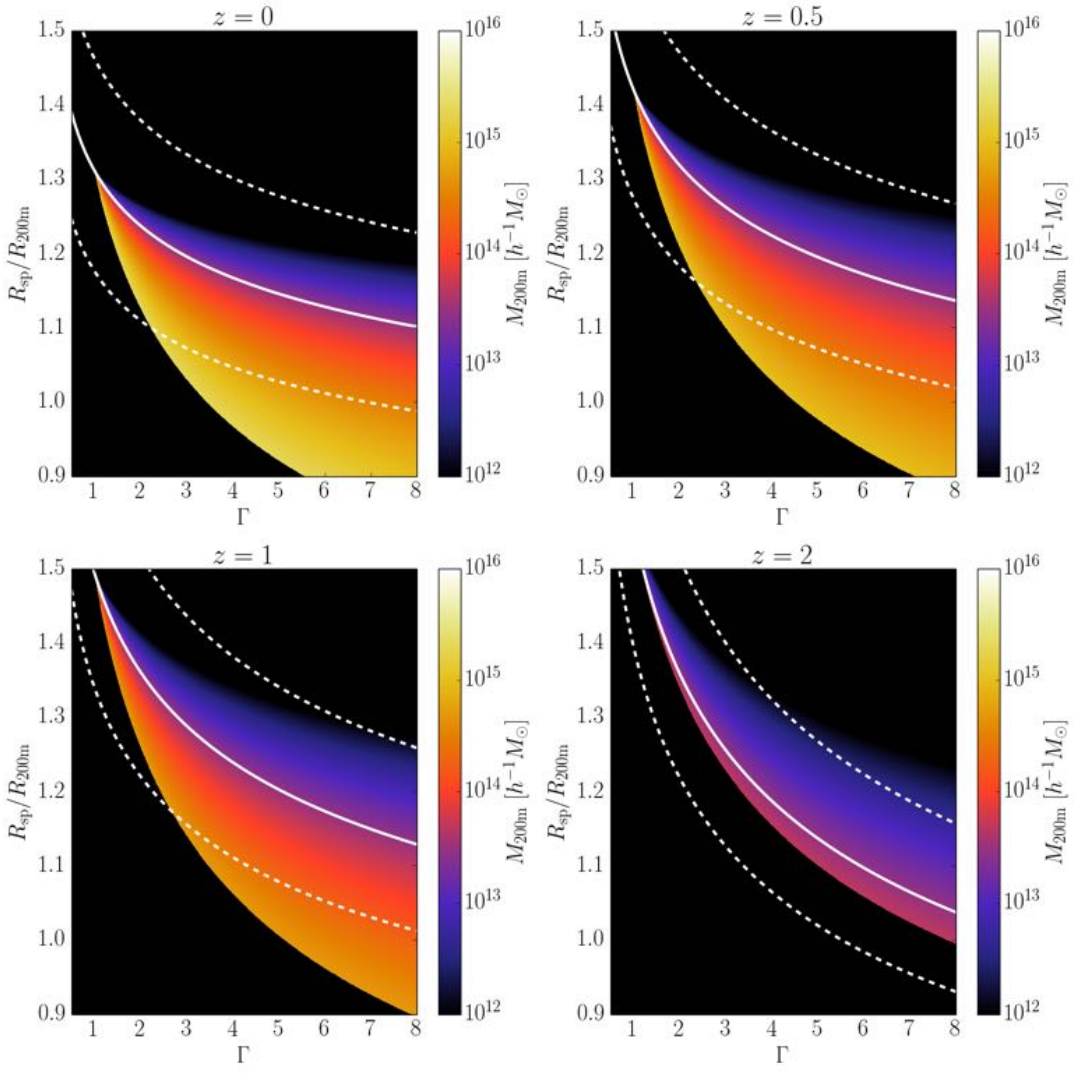

FIG. 8.— The relationship between the median of the fitted $R_{\rm sp}/R_{\rm 200m} \equiv \tilde{R}_{\rm sp}$ distribution and Γ and $M_{\rm 200m}$. Equation 12 has been inverted to displ $M_{\rm 200m}$ as a function of $\tilde{R}_{\rm sp}$ Γ, meaning that $\tilde{R}_{\rm sp,med}(\Gamma)$ at a particular $M_{\rm 200m}$ can be read by following lines of constant color. To visualize the typical wic of of the $\tilde{R}_{\rm sp}$ distribution, dashed white curves showing the 68% contours for $M_{\rm 200m} = 10^{13}\ h^{-1}M_\odot$ and solid white curves showing the median relations f

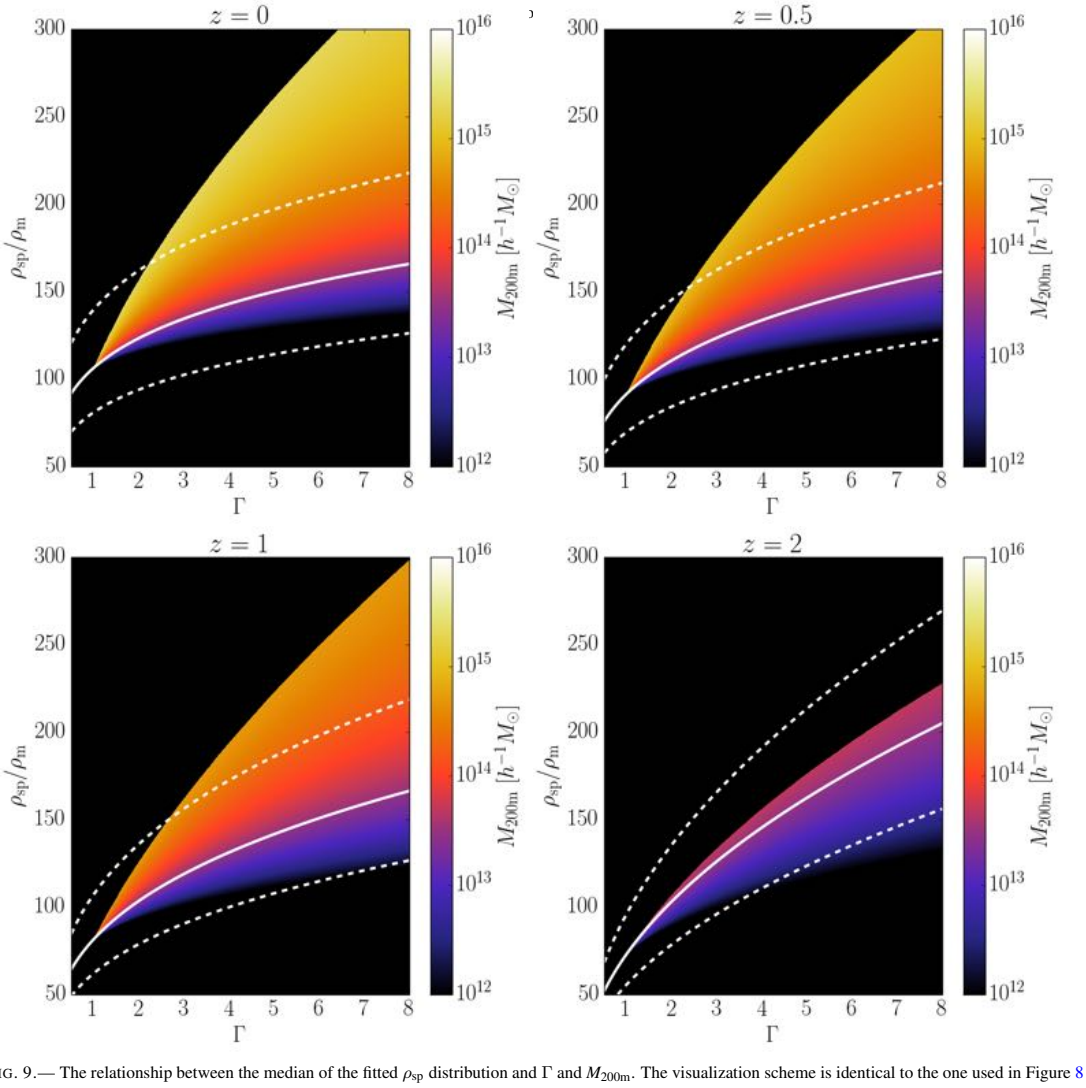

FIG. 9.— The relationship between the median of the fitted $\rho_{\rm sp}$ distribution and Γ and $M_{\rm 200m}$. The visualization scheme is identical to the one used in Figure 8

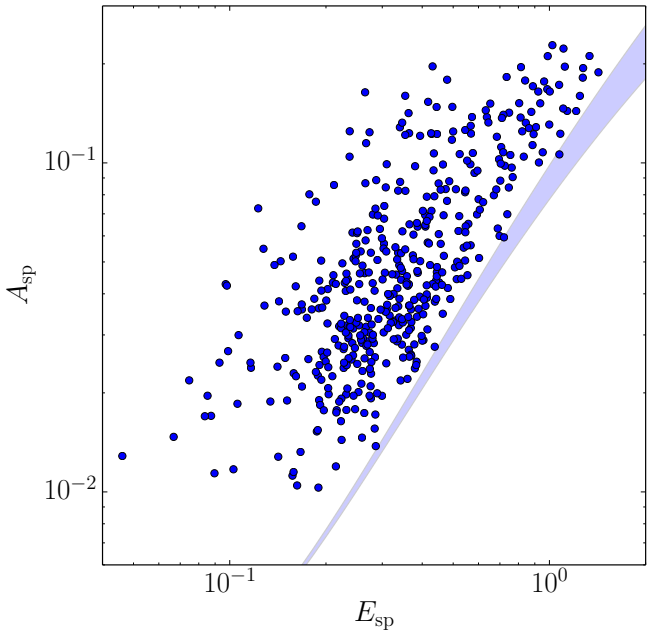

FIG. 10.— The asphericity parameter, $A_{\rm sp}$, versus the ellipticity parameter, $E_{\rm sp}$ (defined in Equations. 11 and Equation 10, respectively) for our $z = 0$ halo sample. The blue shaded region shows the range of values of these quantities for ellipsoids with different axis ratios. The fact that $A_{\rm sp}$ and $E_{\rm sp}$ of the splashback shells lie above the shaded regions means that the shells have significantly higher surface areas than ellipsoids of similar ellipticity and volume.

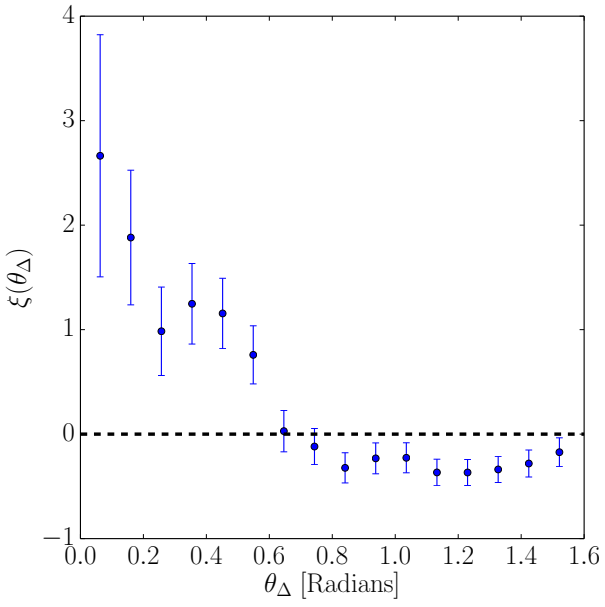

FIG. 11.— The correlation function, $\xi(\theta_\Delta)$, between the major axes of splashback shells and the major axes of total dark matter distribution. The dashed black line shows $\xi(\theta_\Delta) = 0$, and indicates the level of correlation expected for random alignment.